Development Toward Tungsten Transition-Edge Sensors with Improved Energy Resolution in the Optical/NIR Regime

Leaf Swordy, Benedikt Hampel, Daniel S. Swetz, Paul Szypryt, Douglas A. Bennett, Galen O'Neil, Mike Vissers, Joel N. Ullom, Richard P. Mirin, Martin J. Stevens, Adriana E. Lita

***Abstract*—We formulate an energy resolution model for optical transition-edge sensors which combines aspects of existing models with the goal of better defining and constraining energy resolution optimization. The combined model is found to be in better agreement with experimental data, while also allowing for theoretical exploration of phonon trapping for energy resolution enhancement. Additionally, we present preliminary data from our recent low critical temperature (T_c = 50 mK to 100 mK) tungsten Transition Edge Sensors (TESs) for the optical to Near Infra-Red (NIR) regime. Our tungsten TES detectors are shown to exhibit curious 'inverse' proximity effects compared to what is generally reported in the literature. A variety of wiring scheme test structures are analyzed under varying magnetic field shielding conditions in an effort to mitigate and characterize these spurious effects on the device T_c. We develop an electron beam lithography fabrication method in order to reduce the edge roughness of our tungsten TES devices, and demonstrate a more uniform T_c across various TES sizes when these e-beam lithography devices are measured within superconducting magnetic shielding.**

***Index Terms*—Transition Edge Sensor, TES, Superconducting Detectors, Energy Resolution, Astronomy, Phonon Trapping, Habitable Worlds**

I. Introduction

THE Astro2020 priority area, 'Pathways to Habitable Worlds,' highlights the significance of using a space-based telescope equipped with a coronagraph to directly image exoplanets around Sun-like stars and search for signs of life [1]. Extensive research has been performed to understand what spectra of Earth-like exoplanet atmospheres may look like from distant telescopes and identify potential signatures of life. To properly characterize these biosignatures, the detector technology will require a resolving power of $R \approx 100$ ($R = E/\Delta E$) at the 760 nm (O_2 biosignature feature) and wide spectral coverage of 200 nm to 1800 nm, making a future optimized UV-VIS-NIR Transition-Edge Sensor (TES) an excellent detector candidate [2]–[4]. Additionally, because of the extremely low expected count rates over background, the optical/NIR TES's ability to count single photons with high Quantum Efficiency (QE) and few to no dark counts is crucial for this application.

TES detectors consist of a superconducting thin film that is cooled below its critical temperature (T_c), and then biased into the narrow superconducting-to-normal transition region where the temperature coefficient of resistance is extremely high. When a photon is incident on the TES, the minuscule temperature increase upon absorption results in a measurable increase in the device resistance. When the TES is biased at constant voltage, a photon absorption event is seen as a temporary decrease in the device current, or current pulse. By measuring the height and form of this current pulse, a sensitive measurement of the photon energy can be made. Traditionally, the change in TES current has been read out through the use of Superconducting QUantum Interference Devices (SQUIDs) [5], and more recently as demonstrated by our team with a Kinetic Inductance Current Sensor (KICS) [6].

Optical TES devices typically consist of thin superconducting metal films patterned into a square directly on a silicon (Si) substrate (see Fig. 1) and operated at wavelengths from UV to near IR. In these devices, photons are absorbed directly by the electron system of the voltage biased device. At their operating temperatures of $\sim$ 100–200 mK, the Joule heating of the device bias voltage creates a discontinuity between the temperature of the electron gas and that of the lattice due to weak electron-phonon thermal coupling. At this operating point, the temperature spike generated by an absorbed photon decays back to the initial electron temperature with a recovery time on the order of microseconds. The thermal isolation required for calorimetric detection is provided by the weak electron-phonon coupling in the superconductor [7]. Tungsten (W) has weak electron-phonon coupling at cryogenic temperatures and is well suited as an optical TES material.

Recent years have seen advancements for the energy resolution of both TESs and Microwave Kinetic Inductance Detectors (MKIDs) [8]. MKIDs rely on the kinetic inductance of a superconducting microresonator to detect photons; the photosensitive portion of this microresonator circuit is a superconducting inductor. When a photon is absorbed on the inductor, broken Cooper pairs temporarily raise the kinetic inductance of the circuit. This increase in kinetic inductance can be measured as a drop in the MKID resonant frequency, and can be used to count photons while also giving an estimate of the individual photon energies. The ability of MKIDs to resolve the photon energy, coupled with the ease with which MKIDs may be multiplexed, makes them another

Manuscript received March, 2026. This work was supported in part by the NASA APRA program under Grant No. NNH23OB118A and Xanadu Quantum Technologies (https://ror.org/05qj0n416). Author Leaf Swordy (e-mail: leaf.swordy@nist.gov) is a postdoctoral researcher at the National Institute of Standards and Technology, Boulder, Colorado 80305, USA. And part of the Professional Research Experience Program (PREP) with the Department of Physics at the University of Colorado Boulder, Boulder, Colorado 80309,USA.

Authors Benedikt Hampel (e-mail: bnh5@nist.gov), Daniel S. Swetz (e-mail: swetz@nist.gov), Paul Szypryt (e-mail: pns12@nist.gov), Douglas A. Bennett (e-mail: bennettd@nist.gov), Galen O'Neil (e-mail: oneilg@nist.gov), Mike Vissers (e-mail: vissers@nist.gov), Joel N. Ullom (e-mail: ullom@nist.gov), Richard P. Mirin (e-mail: mirin@nist.gov), Martin J. Stevens (e-mail: marty@nist.gov), and Adriana E. Lita (e-mail: adriana.lita@nist.gov) are with the National Institute of Standards and Technology, Boulder, Colorado 80305, USA.

Color versions of one or more of the figures in this article are available online at http://ieeexplore.ieee.org

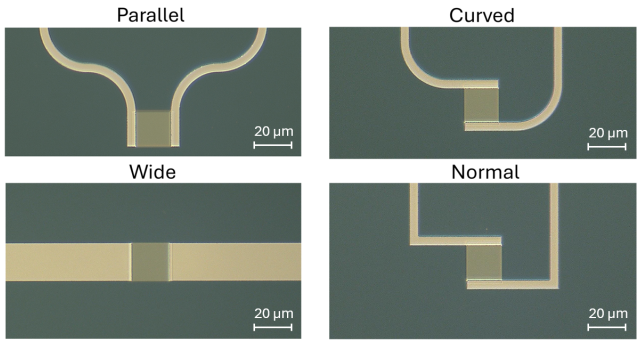

Fig. 1. W TES with varying wire geometry to investigate differences in magnetic self-field and proximity effects of the Nb leads. The 'Normal' scheme is the geometry generally used in our TES devices. The W film thickness is 20 nm, and the thickness of the Nb leads is 80 nm.

prime candidate for future space missions aimed at detecting habitable worlds.

Without any kind of optimization for energy resolution, optical TESs for Quantum Information Science (QIS) applications have demonstrated resolving power $R \approx$ 4-5 at 1550 nm (0.8 eV). Fig. 2 (left) shows TES response to an attenuated 1550 nm pulsed laser showing good photon-number resolution and its corresponding pulse height distribution (right) from which energy resolution is extracted at FWHM. Typically, MKIDs demonstrate resolving power of $R \approx 10$ at the common telecom wavelength of 1550 nm. However, placing MKID devices on membranes and low Debye-temperature bilayers (for phonon trapping enhancement) has recently boosted the resolution to $R \leq 14$ and $R \leq 19$ at 1310 nm and 1550 nm respectively [9], [10]. In the TES case, the current record among published results is $R \leq 12$ at 1550 nm, recently set by Hattori et al. in 2022 [11]. The record was set by fabrication of a low T_c ($\approx$ 115 mK) Au/Ti TES with a small heat capacity. This result is a significant improvement over the standard $R \approx 5$ achieved by TES optimized for 1550 nm light. TES devices however, have demonstrated near-unity system detection efficiencies due to their ease of fabrication within an optical stack that boosts absorption for specific bandwidths.

In these proceedings, we propose an energy resolution model that accounts for resolution degradation arising from both thermal noise considerations and phonon escape statistics. We demonstrate good agreement between model predictions and a limited set of preliminary data while using reasonable values of material/device physical properties. We apply the model to the resolution and bandwidth needs of the Habitable Worlds Observatory (HWO), resulting in new constraints on T_c and phonon trapping to achieve required HWO benchmarks for exoplanet detection. Ultimately, we discuss experimental results of TES behavior for low T_c (from 50 mK to 100 mK) tungsten TES devices, while varying many device parameters to illustrate some unique challenges we have found attempting to fabricate devices in this low T_c regime.

II. Energy Resolution Model

To understand what the limitations are for TES energy resolution, we can look at the theoretical predictions. For a TES, the thermodynamic fluctuations associated with electrical resistance (Johnson noise in the TES resistance and in the bias shunt resistor) and thermal impedance (phonon noise or thermal fluctuation noise (TFN) across the thermal link G that couples the sensor to the bath) represent noise sources that set a fundamental thermodynamic limit on the achievable energy resolution ΔE_{FWHM} of a TES, and can be described as in [12]:

$$\Delta E_{\text{Irwin/Hilton}} = 2.355\sqrt{\frac{4k_B T_c E_{max}}{1+\beta}\sqrt{\frac{nF(T_c,T_b)}{1-(T_b/T_c)^n}}\sqrt{\xi}}, \tag{1}$$

where T_c is TES superconducting transition temperature, T_b is the bath temperature, and $\beta = (I/R)(dR/dI)$ is the sensitivity of the TES resistance to current. In addition, n is the temperature exponent of power flow to the bath, $F(T_c, T_b)$ is a unitless function that describes the relative contribution of the bath to the thermodynamics of the TES, and ξ describes a model for the mixed down Johnson noise [13]. E_{max} is the maximum photon energy to keep the device in the linear regime, $E_{max} = CT_c(1+\beta)/\alpha$, where C is the TES heat capacity and $\alpha = (T/R)(dR/dT)$ is the sensitivity of the TES resistance to temperature.

While the Irwin/Hilton model given in (1) is frequently used, it does not account for a major source of resolution degradation, the statistical variation in energy loss via phonon escape to the substrate following the absorption of a photon. Kozorezov et al. [14] suggests a model to account for phonon losses by introducing the energy collection efficiency κ, as well as the statistical variation in phonon loss $J(E)$:

$$\Delta E_{\text{Kozorezov}} \approx 2.355\sqrt{4k_B T_c^2 C\left(\frac{1}{\alpha}\right)\sqrt{\frac{n}{2}}\frac{1}{\kappa^2} + J(E)E}, \tag{2}$$

Fig. 3 illustrates that the Kozorezov model is far more pessimistic than the Irwin/Hilton model. Even so, the Kozorezov model fails to take into account the thermal noise factor $F(T_c, T_b)$ and Johnson noise factor ξ found in Irwin/Hilton model. While investigating TES energy resolution, we have decided to combine the two models in an attempt to better take all factors of resolution degradation into account:

$$\Delta E_{\text{Irwin/Hilton \& Kozorezov}} \approx 2.355\sqrt{\frac{4k_B T_c E_{max}}{1+\beta}\sqrt{\frac{nF(T_c,T_b)}{1-(T_b/T_c)^n}}\frac{\sqrt{\xi}}{\kappa^2} + J(E)E}, \tag{3}$$

This combined equation is also shown in Fig. 3 (orange dotted curve), and demonstrates very good agreement with our data measured for a W TES device with a T_c of 183 mK, thermal conductance G = 11.1 pW/K and heat capacity C = 0.498 fJ/K. For the TES parameters used to plot (1), (2) and (3) in Fig. 3, we used T_b = 50 mK, β = 5, n = 5, F(T_c, T_b) = 0.6, and ξ = 1 + 2β , reasonable values for our TES devices [12], [15]. The stochastic energy loss into the substrate was represented

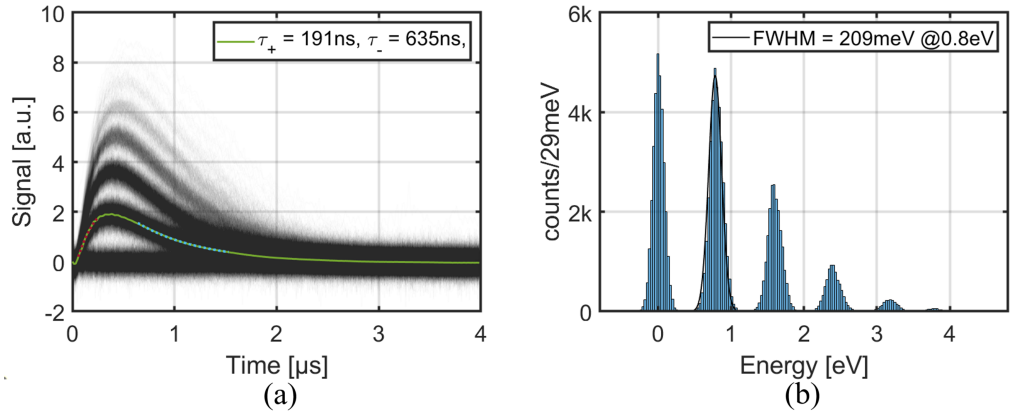

Fig. 2. (a) TES response to 1550 nm attenuated laser pulses and pulse height distribution allowing for FWHM energy resolution measurement (b) for TES device optimized for quantum information applications.

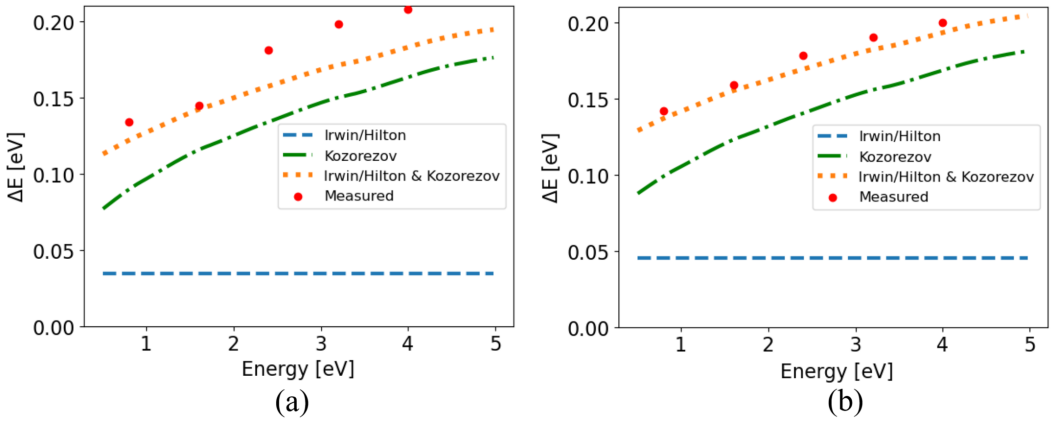

Fig. 3. Results of combining ΔE_{FWHM} models given by Irwin/Hilton and Kozorezov. The combined model (orange dotted curve) takes into account both the thermal fluctuation noise described in the Irwin/Hilton model (blue dashed curve) and the phonon escape/down-conversion noise described in the Kozorezov model (green dashed-dotted curve). Experimental data (red dots) is presented alongside the theoretical resolution curves for a device with $T_c = 154$ mK (a), and $T_c = 183$ mK (b). The combined model is slightly more pessimistic than the regular Kozorezov formulation, and is in better agreement with recent ΔE_{FWHM} measurements of our W TESs. The (b) data demonstrates good agreement with the model with respect to incident photon energy, however, the (a) device was found to deviate from the model significantly, whether this indicates a broader T_c scaling discrepancy with the model remains to be seen. Although the lower T_c device is not in as good agreement with combined model as the higher T_c device, overall the combined model fits better, at least at lower energy levels.

as $\kappa = 0.36$ and $J(E) = 1.22 \times 10^3$ in line with literature values [14].

This model also allows us to simulate the effects of phonon trapping by varying the factors κ and $J(E)$ ($\kappa \to 1$ and $J(E) \to 0$), which represents capturing a greater fraction of the incident photon as thermal energy in the electron system of the device. Fig. 4 demonstrates that phonon trapping moves the curves from the Irwin/Hilton & Kozorezov model, to the more ideal Irwin/Hilton model ($\kappa = 1$ and $J(E) = 0$). We have also plotted results from W TES detectors both without (red) and with (blue) phonon trapping on membranes. While we are currently far from the ideal situation of 100% phonon trapping, there are many strategies to improve and get closer to the upper limit of TES resolution.

III. Measurements of Low T_c W TES

It is clear from Fig. 4 that in order to achieve energy resolution approaching the requirements of exoplanet spectroscopy ($R \approx 100$), there must be significant improvements in phonon trapping as well as a significant reduction of the critical temperature. Here we explore some recent preliminary results to achieve lower T_c tungsten TES.

In the past we have demonstrated tuneable T_c by varying the fraction of α ($T_c \approx 15$ mK) and β ($T_c = 1 - 4$ K) crystallographic phases of tungsten by modifying thin film deposition parameters (e.g. pressure/sputtering power) [16]. Using these methods, we have been very successful in achieving films with T_c in the range of 50 mK to 100 mK. However, when etched into smaller geometries required for optical TES devices (20 μm × 20 μm), we find that the T_c is significantly suppressed, with many devices remaining in the normal state down to the base temperature of our Adiabatic Demagnetization Refrigerator (ADR) cryostat (30 mK). This result (see Fig. 5) is in contradiction with the trend observed in other TES devices (e.g. molybdenum gold TESs), which typically demonstrate an increase in T_c with reduced device area [17] (generally attributed to proximity effects from the

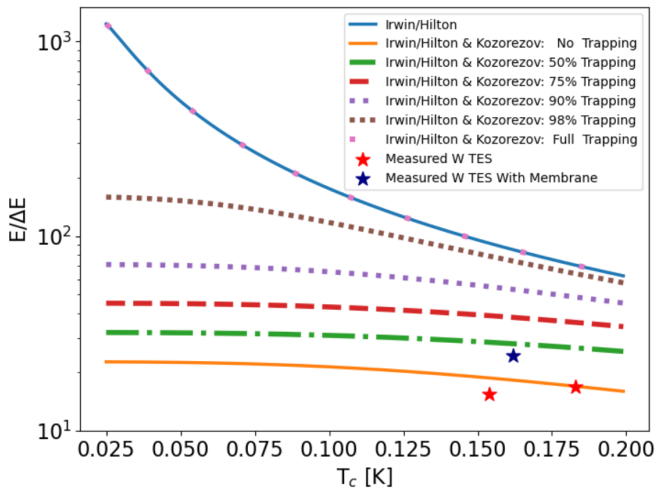

Fig. 4. Varying the energy collection efficiency κ, as well as the phonon-escape noise factor $J(E)$, allows us to estimate how close to the ideal Irwin/Hilton model (blue curve) we can feasibly get using phonon trapping methods (e.g. membranes and/or low-Debye temperature substrates). At 0% trapping $\kappa = 0.36$ and $J(E) = 1.22 \times 10^3$ (unitless), which is in line with values from the literature [14]. At 100% trapping, $\kappa = 1$ and $J(E) = 0$, representing zero energy loss to the substrate in the form of phonons. The curves at intermediate degrees of trapping are created by increasing κ and reducing $J(E)$ by the specified percentage, a natural method given that both parameters are directly proportional to the amount of energy captured by the TES as thermal energy. Included are three data points from recent W TES devices measured by our group, both with and without membranes (the blue star device is suspended on a 500 nm silicon nitride membrane). The two red stars are the 3.2 eV datapoints for the (a) and (b) devices of Fig. 3. The model assumes a W TES and a 3.2 eV (387.4 nm) incident photon.

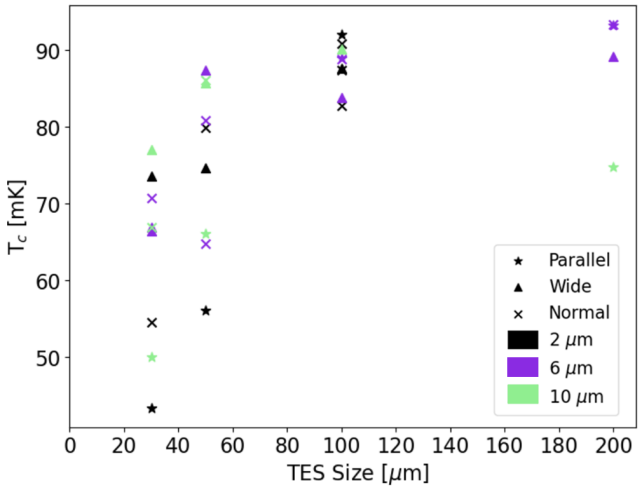

Fig. 5. Measured critical temperature of a low T_c (∼90 mK) film as a function of the TES size. The data demonstrates reduced T_c for smaller TES sizes. 10 μm and 20 μm TES devices were also tested, but are not shown on the plot because they did not superconduct down to the ADR cryostat base temperature of 30 mK. The effects of varying Nb wire overlap on the W square from 2 μm to 10 μm on the T_c is also shown, though the results are somewhat inconclusive.

superconducting wire leads). In order to investigate proximity effects by the Nb leads on our devices, as well as possible interactions with the 'self-field' induced by the bias current, we fabricated a variety of wiring schemes with TES side lengths in the range of 10 μm -100 μm. Fig. 1 shows four different wiring schemes three of which are plotted in Fig. 5 (there was no measurable distinction between the 'Normal' and 'Curved' geometries, so the 'Curved' data is omitted), all devices shown in the microscope images are 20 μm × 20 μm.

Fig. 5 demonstrates reduction of T_c with reduced device area, with the behavior being fairly consistent across all wiring schemes. These results were obtained using a W film deposition tuned to a T_c of ∼ 90 mK. The device T_c was determined by slow variation of the ADR cryostat temperature while applying very small bias current (∼ 1 μA). The transition temperature is defined as 50% R_N on a fitted sigmoid function to the bias signal SQUID output. Each resistance measurement was taken as the average of eight samples at a given fixed cryostat temperature, and each data point in the plot represents the 50% R_N found by fitting data from a single device for a single temperature sweep of the cryostat. The most notable takeaway of Fig. 5 is that no 10 μm or 20 μm devices superconduct. Under 30 μm the superconducting state appears to be fully suppressed, a significant issue given that a device achieving $R \approx 100$ would likely need to be 20 μm or smaller.

In addition to T_c scaling with device geometry, Fig. 5 also explores the effect of the Nb wire overlap region on the transition temperature. Our standard W TES utilizes a 2 μm wire overlap area, serving as the boundary for a symmetrical 20 μm × 20 μm optical absorption region that does not include the overlap region, as illustrated in our Fig. 1 images. The black, purple, and green data of Fig. 5 represent wire overlap areas of 2 μm, 6 μm, and 10 μm, respectively. Although the 10 μm wire overlap data (green) generally featured slightly higher T_c than the equivalent wiring scheme at 2 μm overlap (black). The results are not consistent enough to draw a solid conclusion. The persistence of suppressed T_c for smaller sizes, even for the case of 10 μm wire overlap, seems to indicate that proximity from the leads is not the principal influence on the T_c scaling.

IV. Effects of Local Magnetic Fields

Due to significant variation of T_c for various TES devices from the same fabrication run and sometimes from different cooldown to cooldown, we started implementing external magnetic shielding. Fig. 6 demonstrates that, when a superconducting lead shield is used in addition to external μ-metal shielding (green data), the overall device T_c is raised for all device sizes. Additionally, the trend of reduced T_c with smaller device size is significantly mitigated by magnetic shielding. These results imply a strong B-field dependence of the T_c suppression, possibly due to a reduced barrier to vortex entry, or influences on the supercurrent density flowing through the TES. Interactions between the magnetic field and other device parameters (e.g. edge roughness), are discussed in Section V. Although low-T_c devices are the goal for future high energy resolution devices, the T_c suppression brought about by incident B-fields is inconsistent. The results of Fig. 6 indicate that high energy resolution low-T_c W TES will likely require magnetic shielding in order to maintain a repeatable T_c in the 50 mK to 100 mK range.

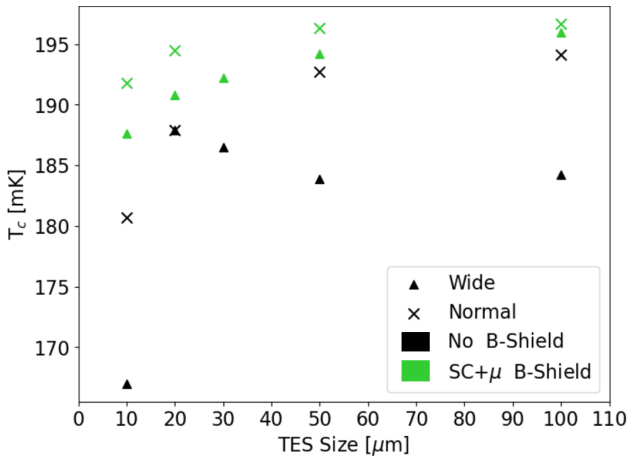

Fig. 6. Effects of applying a superconducting lead shield around the devices in combination with an external μ metal shield. In addition to a raised device T_c across all TES sizes, the reduction in T_c for reduced device size is seen to be significantly mitigated by the magnetic shielding. For any wiring scheme at a given size, the black/green data are the same exact device placed in different shielding scenarios.

V. Reduced Edge Roughness Effects on Low T_c TES Devices

As the lateral dimensions of a TES are reduced, effects associated with the device edges naturally become more relevant compared to effects arising from the inner area of the TES (due to strictly geometric arguments). Therefore, edge effects are a likely candidate for causing the B-field induced T_c suppression observed in Fig. 5. To investigate this possibility, we are currently developing fabrication methods to smooth the edges of our W TES devices.

Using e-beam lithography techniques, as opposed to the photolithography generally used to produce our W TES devices, immediately produces a much smoother edge, which can be seen in the Scanning Electron Microscopy (SEM) images shown in Fig. 7. These devices feature a raised T_c compared to devices fabricated with our normal process (Fig. 8, blue vs. black data), while also appearing to exhibit less suppression of T_c as the size of the TES is reduced. It is worth noting that, when the edge roughness is reduced and superconducting shielding is used, the 10 μm and 20 μm devices are now superconducting, whereas they were not in Fig. 5. There are gains in T_c for the 30 μm × 30 μm and 20 μm × 20 μm TES devices (Fig. 8, green data), as well as reduced spread in T_c data. Future measurements are needed to determine the energy resolution of these low T_c TES devices, and to test whether the gains align with our newly formulated model of energy resolution.

VI. Conclusion

We have demonstrated a variety of TES characteristics related to achieving a higher energy resolution for astronomy and QIS applications. We have also presented preliminary data taken on our low T_c W TES devices. Key takeaways from this proceedings include:

- To better constrain device parameters for optimizing energy resolution, we developed a hybrid model for energy resolution combining the thermal noise model of Irwin/Hilton with phonon loss models of Kozorezov.
- The combined Irwin/Hilton & Kozorezov model was used to extrapolate the required levels of phonon trapping to achieve key energy resolution benchmarks for the Habitable Worlds Observatory. We found that high degrees of phonon trapping ($> 90\%$) in combination with low device T_c (50 - 100 mK) may be required to approach the HWO benchmark resolution ($R \approx 100$).
- Variation of TES superconducting transition temperature, T_c, was explored for a variety of different wiring schemes and detector geometries with the goal of improved energy resolution.
- Implementation of a superconducting magnetic shield, in addition to an external μ−metal shield, eliminated a lot of the unexplained T_c variation and T_c suppression especially for smaller size TES devices.
- A new fabrication process utilizing e-beam lithography was developed to reduce edge-roughness of our W TES devices. The e-beam process demonstrated a much smoother edge of the tungsten square of the TES device, and led to TES devices with raised T_c when compared to devices fabricated via photolithography.

While much of the data presented here is preliminary, we have demonstrated progress towards characterizing both the theoretical and physical constraints required to achieve W TES devices with improved energy resolution. We have reported on characteristics of low T_c optical/NIR W TES devices, as well as strategies for alleviating spurious influence of proximity effect and magnetic interference.

References

[1] National Academies of Sciences, Engineering, Medicine *et al.*, *Pathways to Discovery in Astronomy and Astrophysics for the 2020s*. The National Academies Press Washington, DC, 2021.

[2] B. J. Rauscher, M. R. Bolcar, M. Clampin, S. D. Domagal-Goldman, M. W. McElwain, S. H. Moseley, C. Stahle, C. C. Stark, and H. A. Thronson, "ATLAST detector needs for direct spectroscopic biosignature characterization in the visible and near-IR," in *UV/Optical/IR Space Telescopes and Instruments: Innovative Technologies and Concepts VII*. United States, 2015, p. 96020D, doi: 10.1117/12.2186554.

[3] P. C. Nagler, M. A. Greenhouse, S. H. Moseley, B. J. Rauscher, and J. E. Sadleir, "Development of transition edge sensors optimized for single-photon spectroscopy in the optical and near-infrared," in *High Energy, Optical, and Infrared Detectors for Astronomy VIII*, Austin, United States, 2018, p. 117, doi: 10.1117/12.2313730.

[4] P. C. Nagler, J. E. Sadleir, and E. J. Wollack, "Transition-edge sensor detectors for the origins space telescope," *Journal of Astronomical Telescopes, Instruments, and Systems*, vol. 7, p. 011005, Jan 2021, doi: 10.1117/1.JATIS.7.1.011005.

[5] R. C. Jaklevic, J. Lambe, A. H. Silver, and J. E. Mercereau, "Quantum interference effects in josephson tunneling," *Phys. Rev. Lett.*, vol. 12, pp. 159–160, Feb 1964, doi: 10.1103/PhysRevLett.12.159.

[6] P. Szypryt, D. A. Bennett, I. F. Florang, J. W. Fowler, A. Giachero, R. Hummatov, A. E. Lita, J. A. B. Mates, S. W. Nam, G. C. O'Neil, D. S. Swetz, J. N. Ullom, M. R. Vissers, J. Wheeler, and J. Gao, "Kinetic inductance current sensor for visible to near-infrared wavelength transition-edge sensor readout," *Communications Engineering*, vol. 3, p. 160, Nov 2024, doi: 10.1038/s44172-024-00308-y.

[7] B. Calkins, A. E. Lita, A. E. Fox, and S. Woo Nam, "Faster recovery time of a hot-electron transition-edge sensor by use of normal metal heat-sinks," *Applied Physics Letters*, vol. 99, no. 24, p. 241114, Dec 2011, doi: 10.1063/1.3659686.

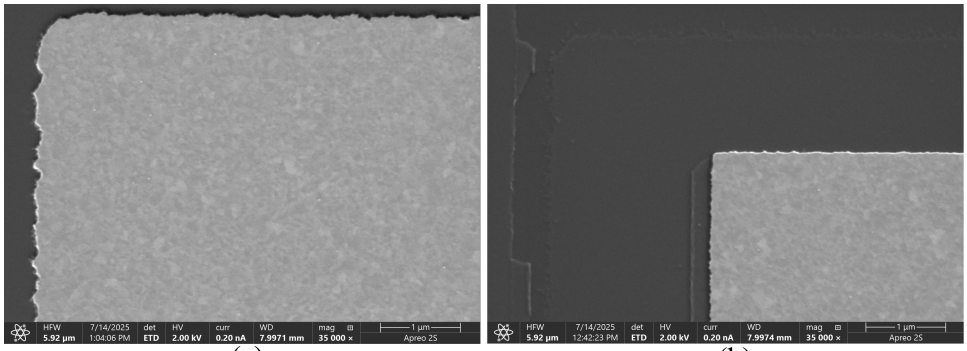

Fig. 7. SEM micrographs of TES devices produced by our regular process of photolithography and W wet-etch (a), and the same film patterned with e-beam lithography followed by W wet etch (b). The edge is visibly smoother for the e-beam lithography fabrication, though there is still some visible roughness as a result of the wet-etch. Both images feature 35,000× magnification.

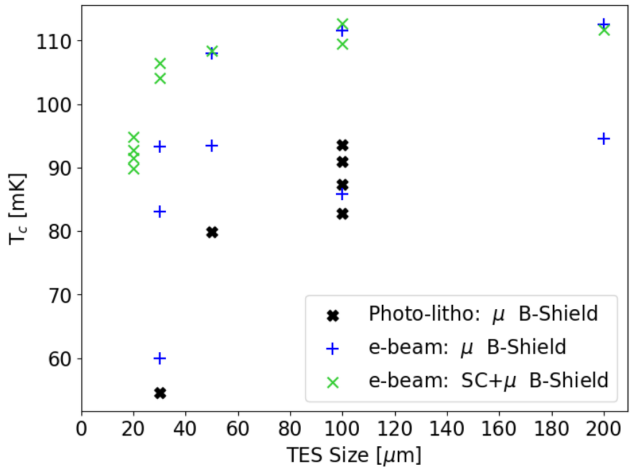

Fig. 8. Comparison between our regular photolithography TES fabrication on a low T_c film (black data), the same film recipe fabricated with e-beam lithography (blue data), as well as the effect of placing the e-beam devices inside a superconducting lead shield in addition to the external μ-metal shield (green data). A general trend can be seen that the e-beam devices feature increased T_c across all sizes, and the SC lead shield pushes the 20 μm × 20 μm devices to superconduct (though they were present in the test, no 20 μm × 20 μm devices superconducted down to 30 mK for the black or blue data). All devices shown in this plot utilized the 'Normal' wiring scheme.

[8] P. K. Day, H. G. LeDuc, B. A. Mazin, A. Vayonakis, and J. Zmuidzinas, "A broadband superconducting detector suitable for use in large arrays," *Nature*, vol. 425, pp. 817–821, Mar 2003, doi: 10.1038/nature02037.

[9] N. Zobrist, W. H. Clay, G. Coiffard, M. Daal, N. Swimmer, P. Day, and B. A. Mazin, "Membraneless Phonon Trapping and Resolution Enhancement in Optical Microwave Kinetic Inductance Detectors," *Phys. Rev. Lett.*, vol. 129, no. 1, p. 017701, Jul 2022, doi: 10.1103/PhysRevLett.129.017701.

[10] P. J. de Visser, S. A. de Rooij, V. Murugesan, D. J. Thoen, and J. J. Baselmans, "Phonon-trapping-enhanced energy resolution in superconducting single-photon detectors," *Phys. Rev. Appl.*, vol. 16, p. 034051, Sep 2021, doi: 10.1103/PhysRevApplied.16.034051.

[11] K. Hattori, T. Konno, Y. Miura, S. Takasu, and D. Fukuda, "An optical transition-edge sensor with high energy resolution," *Superconductor Science and Technology*, vol. 35, p. 095002, sep 2022, doi: 10.1088/1361-6668/ac7e7b.

[12] K. D. Irwin and G. C. Hilton, *Transition-Edge Sensors*. Berlin, Germany: Springer, 2005, vol. 99.

[13] A. Wessels, K. Morgan, J. D. Gard, G. C. Hilton, J. A. B. Mates, C. D. Reintsema, D. R. Schmidt, D. S. Swetz, J. N. Ullom, L. R. Vale, and D. A. Bennett, "A model for excess johnson noise in superconducting transition-edge sensors," *Applied Physics Letters*, vol. 118, p. 202601, May 2021, doi: 10.1063/5.0043369.

[14] A. G. Kozorezov, J. K. Wigmore, D. Martin, P. Verhoeve, and A. Peacock, "Resolution limitation in superconducting transition edge photon detectors due to downconversion phonon noise," *Applied Physics Letters*, vol. 89, p. 223510, Nov 2006, doi: 10.1063/1.2397016.

[15] R. Hummatov, A. E. Lita, T. Farrahi, N. Otrooshi, S. Fayer, M. J. Collins, M. Durkin, D. Bennett, J. Ullom, R. P. Mirin, and S. Woo Nam, "Fast transition-edge sensors suitable for photonic quantum computing," *Journal of Applied Physics*, vol. 133, no. 23, p. 234502, Jun. 2023, doi: 10.1063/5.0149478.

[16] A. Lita, D. Rosenberg, S. Nam, A. Miller, D. Balzar, L. Kaatz, and R. Schwall, "Tuning of tungsten thin film superconducting transition temperature for fabrication of photon number resolving detectors," *IEEE Transactions on Applied Superconductivity*, vol. 15, no. 2, pp. 3528–3531, Jan. 2005, doi: 10.1109/TASC.2005.849033.

[17] J. E. Sadleir, S. J. Smith, I. K. Robinson, F. M. Finkbeiner, J. A. Chervenak, S. R. Bandler, M. E. Eckart, and C. A. Kilbourne, "Proximity effects and nonequilibrium superconductivity in transition-edge sensors," *Phys. Rev. B*, vol. 84, p. 184502, Nov 2011, doi: 10.1103/PhysRevB.84.184502.